

Article

Enhancing Additive Restoration of Damaged Polymer Curved Surfaces through Compensated Support Beam Utilization

Dianjin Zhang ^{1,2,*} and Bin Guo ¹

¹ School of Materials Science and Engineering, Harbin Institute of Technology, Harbin 150001, China; bguo@hit.edu.cn

² Zhengzhou Research Institute, Harbin Institute of Technology, Zhengzhou 450000, China

* Correspondence: zhangdianjin@hit.edu.cn

Abstract: As additive manufacturing advances, it offers a cost-effective avenue for structurally repairing components. However, a challenge arises in the additive repair of suspended damaged surfaces, primarily due to gravitational forces. This can result in excessive deformation during the repair process, rendering the formation of proper repair impractical and leading to potential failure. In light of this rationale, conventional repair techniques are impractical for extensively damaged surfaces. Thus, this article proposes a novel repair methodology that is tailored to address large-area damage. Moreover, and departing from conventional practices involving the addition and subsequent subtraction of materials for precision machining, the proposed process endeavors to achieve more precise repair outcomes in a single operation. This paper introduces an innovative repair approach employing fused deposition modeling (FDM) to address the complexities associated with the repair of damaged polymer material parts. To mitigate geometric errors in the repaired structural components, beams with minimal deformation are printed using a compensation method. These beams then serve as supports for overlay printing. The paper outlines a methodology by which to determine the distribution of these supporting beams based on the shape of the damaged surface. A beam deformation model is established, and the printing trajectory of the compensated beam is calculated according to this model. Using the deformation model, the calculated deformation trajectories exhibit excellent fitting with the experimentally collected data, with an average difference between the two of less than 0.3 mm, validating the accuracy of the suspended beam deformation model. Based on the statistical findings, the maximum average deformation of the uncompensated sample is approximately 5.20 mm, whereas the maximum deformation of the sampled point after compensation measures around 0.15 mm. Consequently, the maximum deformation of the printed sample post-compensation is mitigated to roughly 3% of its pre-compensation magnitude. The proposed method in this paper was applied to the repair experiment of damaged curved surface components. A comparison was made between the point cloud data of the repaired surface and the ideal model of the component, with the average distance between them serving as the repair error metric. The mean distance between the point clouds of the repaired parts using the proposed repair strategy is 0.197 mm and the intact model surface is noticeably less than the mean distance corresponding to direct repair, at 0.830 mm. The repair error with compensatory support beams was found to be 76% lower than that without compensatory support beams. The surface without compensatory support beams exhibited gaps, while the surface with compensatory support beams appeared dense and complete. Experimental results demonstrate the effectiveness of the proposed method in significantly reducing the geometric errors in the repaired structural parts. The outcomes of the FDM repair method are validated through these experiments, affirming its practical efficacy. It is noteworthy that, although only PLA material was used in this study, the proposed method is general and effective for other polymer materials. This holds the potential to significantly reduce costs for the remanufacturing of widely used polymers.

Keywords: additive repair; damaged surfaces; support beam; compensated method



Citation: Zhang, D.; Guo, B.

Enhancing Additive Restoration of Damaged Polymer Curved Surfaces through Compensated Support Beam Utilization. *Processes* **2024**, *12*, 393. <https://doi.org/10.3390/pr12020393>

Academic Editors: Diane Mynors and Qingping Yang

Received: 19 January 2024

Revised: 9 February 2024

Accepted: 14 February 2024

Published: 16 February 2024



Copyright: © 2024 by the authors. Licensee MDPI, Basel, Switzerland. This article is an open access article distributed under the terms and conditions of the Creative Commons Attribution (CC BY) license (<https://creativecommons.org/licenses/by/4.0/>).

1. Introduction

In recent years, the application of additive manufacturing in the field of repair has garnered increasing attention from researchers, owing to its notable advantages of rapidity, convenience, efficiency, and facile automatic control [1–3]. Additive repair techniques have found widespread utilization in diverse areas, including, but not limited to, aero-engine blade restoration [4], the repair of damaged ships [5], and cranial reconstruction [6].

However, a recurrent challenge encountered in additive repair processes is the phenomenon known as “hanging printing,” wherein the influence of gravity results in material sinking, the prevention of optimal adhesion or, in cases of extended hanging distances, impedance of material formation [7–9]. To address this issue, a conventional approach to additive manufacturing has been developed that involves the incorporation of support structures. Specifically, on sections of the print with significant overhangs, researchers advocate the preliminary printing of sparse support materials. This strategic measure serves to diminish overhang distances, thereby ensuring a seamless and successful printing process. Researchers have employed multi-degree-of-freedom printing devices to manipulate the orientation of the printed object, ensuring that the printing position remains consistently non-suspended [10–12]. This approach mitigates the influence of gravity during the printing process.

While these methods have proved to be effective in conventional additive manufacturing scenarios, they present limitations when applied to the additive repair of damaged thin-walled surfaces. The interference of printing equipment with compromised surfaces often complicates the insertion of supporting materials within the damaged areas. Furthermore, due to this interference, even with adjustments to the posture of the damaged surface, selecting an optimal angle to overcome the influence of gravity and successfully print and repair the damaged portions becomes a formidable challenge.

Currently, prevalent additive manufacturing methods for repair encompass powder bed fusion, directed energy deposition, and cold spray additive manufacturing. B. Merz et al. [13] conducted the repair of gas turbine blades utilizing laser powder bed melting technology. With the aim of overcoming the technical challenge of the irrecoverable loss of mechanical properties caused by the high heat input of traditional fusion welding, Hamilton et al. [14] determined different parameters for directed energy deposition (DED), maximizing the strength and fatigue life of repaired cast iron, while A. Saboori et al. [15] explored the application of directed energy deposition in the repair process. Lang et al. [16] investigated the cold gas spraying repair process for high-temperature alloy Inconel 718 components. Metallographic examinations revealed a well-bonded interface between the repair filler and the base material. L.P. Martin et al. [17] repaired an aluminum 6061 plate using additive friction stir deposition.

Another potential way to overcome the deformation of the suspended printing area caused by gravity is to utilize the shape memory effect of the printing material. Rahmatabadi et al. [18] printed PLA–TPU blends with different component ratios using melt mixing and melt deposition modeling (FDM), studied the shape memory effect of the polymer, and conducted a detailed material performance analysis of the PLA–TPU mixture [19]. Moreover, in terms of enhancing repair strength, material modification emerges as a promising strategy. Rahmatabadi et al. [20] enhanced the thermal stability and tensile strength of PVC through modification techniques. This advancement enabled the 3D printing of pure, food-grade PVC, which holds the potential for use in biomedical applications. Considering its advantageous attributes of affordability and robust mechanical properties, modified PVC material emerges as a suitable candidate for additive repair.

Notably, the focus of these repair studies predominantly revolves around metallic components, with limited exploration into non-metal parts. Given the widespread utilization of polymer materials, addressing the repair of polymer components could yield substantial cost and time savings compared with reproducing corresponding items. In addition, traditional support printing processes are not suitable for repair scenarios where internal support cannot be added. Therefore, for large-area, damaged, thin-walled polymer parts, new processes and methods must be proposed for their repair. Of particular significance is

the unresolved challenge of “hanging printing” in the additive repair of damaged curved surfaces, an issue not yet adequately addressed in current research.

To overcome the challenge of repairing large-area damaged curved surfaces in additive manufacturing processes, a novel additive repair method using compensatory beams is proposed for the first time. This method not only achieves the unsupported repair of large, damaged areas but also strives to maintain the original appearance of the component as much as possible. This paper introduces a research initiative focusing on the restoration of complex, damaged curved surfaces composed of polymer materials. In contrast with alternative additive manufacturing methods, fused deposition modeling (FDM) offers distinct advantages, such as cost-effectiveness and straightforward manufacturing apparatus and processes, and minimal environmental requirements [21]. Its suitability for the in-situ or ex-situ repair of damaged polymer components makes it a compelling choice. Taking these considerations into account, this paper proposes an FDM-based repair strategy. Initially, a support beam with minimal deformation is produced using a compensation method. Subsequently, the covering layer is applied to the support beam, effectively managing the deformation of the repair surface and ensuring a secure adhesion between the covering lines. The paper will focus on modeling and compensation methods for the deformation patterns of support beams, as well as detailed discussions on layer trajectory planning.

2. Methods

An inherent challenge encountered during the fused deposition modeling (FDM) process for polymer repair is the pronounced influence of gravity on the extruded filament, leading to evident deformation of the repair surface, as depicted in Figure 1a, or inadequate bonding between filament lines, as illustrated in Figure 1b. Figure 1c highlights the proposed solution, involving the printing of precise support beams followed by overlay printing, effectively mitigating the impact of gravity and ensuring optimal bonding for successful polymer repair.

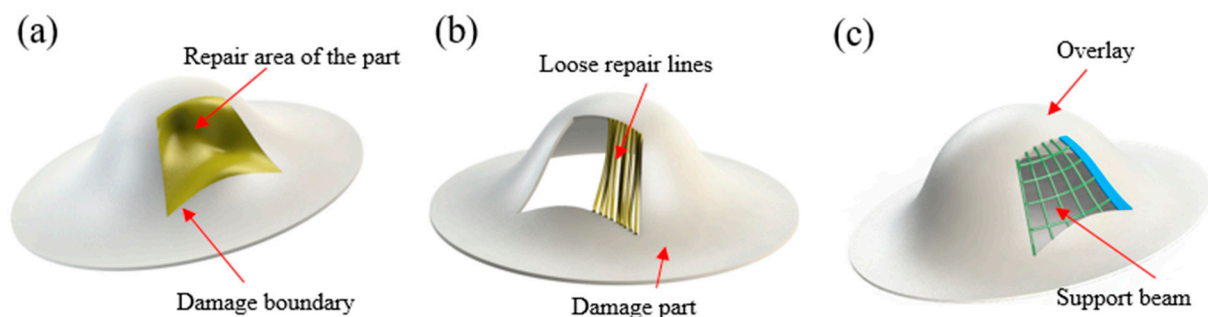


Figure 1. (a) The deformation observed in fused deposition modeling (FDM) repaired components affected by gravity. (b) A lack of effective bonding between the printed lines is evident. (c) The FDM repair strategy, involving the initial printing of support beams followed by overlay printing on the beams.

Figure 2 illustrates the comprehensive fused deposition modeling (FDM) repair process in detail. Initially, the damaged parts’ surfaces undergo scanning with a structured light scanner, followed by a fitting of the surface based on the acquired point cloud. The point cloud of the damaged component as a whole is obtained through multiple scans using a 3D scanner, followed by filtering and registration. The scanner resolution is set at 0.01 mm, ensuring the accuracy of scanning for the damaged components. The disparity between the fitted surface and the complete 3D model is registered and computed to determine the damaged area surface of the parts slated for repair. The damaged area surface is projected onto an optimal plane to derive the plane contour. For this contour, the distribution of support beams is ascertained on the plane. Subsequently, the distribution of support beams on the plane is re-projected onto the surface to establish the support beam distribution at

the damaged part. Employing the compensation method, support beams are printed onto the damaged surface. The scanning direction is defined, and the covering layer for the damaged parts is printed on the support beam. To enhance the bonding strength between the repaired and damaged parts, the covering layer is positioned to maximize contact with the boundary. The scanning direction of the covering layer aligns with the vertical direction of the principal component of the projected contour of the damaged surface.

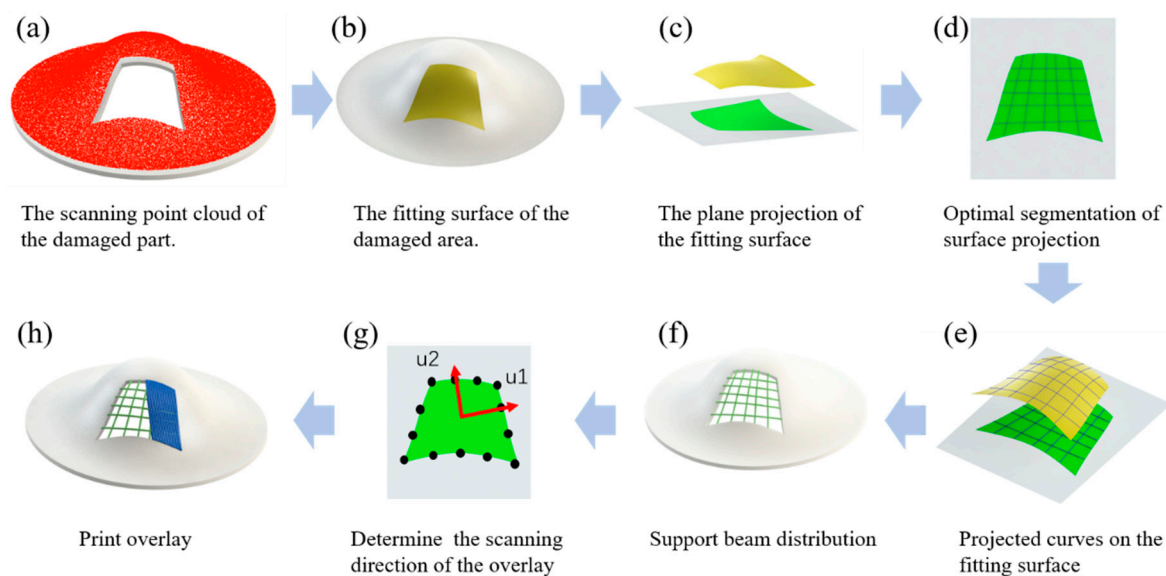


Figure 2. Repairing damaged components: a procedural analysis. (a) Utilize a 3D scanner to capture a point cloud representation of the damaged components. (b) Employ surface fitting techniques to model the damaged area based on its surrounding morphology. (c) Project the fitted damaged contour onto a specified plane. (d) Execute optimal segmentation techniques on the projected plane area. (e) Transfer the segmentation information from the plane onto the damaged surface. (f) Generate support beams derived from segmented contours. (g) Determine the printing orientation for overlay application. (h) Implement overlay printing onto the damaged component.

The repair scheme faces two challenges: determining the distribution of beams in the damaged area and achieving the printing of support beams with minimal deformation. This article will concentrate on addressing these two pivotal issues.

2.1. The Distribution of Support Beams

The support beam plays a crucial role in managing line deformation during the hanging printing process, ensuring it remains within an acceptable range. This paper introduces the concept of the effective suspension distance, denoting the maximum distance a line can suspend with acceptable deformation. The effective suspension distance is contingent on factors such as printing material, nozzle size, cooling rate, and acceptable deformation range. To adapt to specific printing tasks, experimental testing is necessary to ascertain the effective suspension distance, emphasizing the need to maintain a support beam spacing that is less than this critical distance. This principle underscores the importance of minimizing support beams while guaranteeing that the printing of the covering layer falls within the effective hanging distance.

Given the complexity and diversity of surfaces, describing them in a unified mathematical language proves challenging, making support beam determination difficult. This paper employs a method of projecting the surface onto a plane for processing. The selection of the plane is critical, aiming to minimize changes in line distribution after their projection onto the surface. The optimal projection plane is identified as that with the largest surface projection contour area, as determined by the principles of projection geometry [22]. The

finite difference [23] and Adagrad gradient descent algorithm [24] are employed in this study to maximize the projected surface area and determine the optimal projection plane.

The projection vector n of the surface can be defined by two parameters, denoted as α and β and illustrated in Figure 3. The objective is to find optimal values for α and β that maximize the projected area. The algorithm is outlined as follows (Algorithm 1):

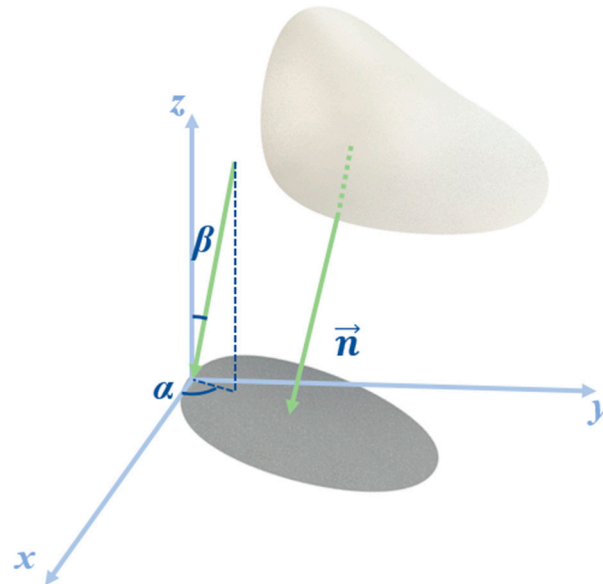


Figure 3. The surface is projected onto a designated plane, with the normal vector n of the projection plane determined by two parameters, denoted as α and β .

Algorithm 1: Optimal projection plane search algorithm

Initialize α, β randomly within the search range
 Given learning rate e and maximum search times n
 Given finite difference wave momentum $\Delta\theta$

While the maximum number of searches was not reached

 Calculate the projected area S_0 of the surface according to (α, β)

 Calculate the projected area $S_{\alpha1}$ of the surface according to $(\alpha + \Delta\theta, \beta)$

 Calculate the projected area $S_{\beta1}$ of the surface according to $(\alpha, \beta + \Delta\theta)$

 Estimate the gradient $\mathbf{Grad} = [S_{\alpha1} - S_0/\Delta\theta, S_{\beta1} - S_0/\Delta\theta]$

$R = R + \mathbf{Grad}^2$

 Update α, β :

$$\alpha = \alpha + e \times \mathbf{Grad}[1]/(\Delta\theta + \text{sqrt}(R))$$

$$\beta = \beta + e \times \mathbf{Grad}[2]/(\Delta\theta + \text{sqrt}(R))$$

end

Following the identification of the optimal projection plane, it becomes imperative to ascertain the positioning of the support beam on this plane. Initially, the endpoints of support beam segments are uniformly distributed along the surface projection contour. Subsequently, endpoints are selected based on the optimization of the objective function, defined as follows:

$$F = k_1 L_m + k_2 L_\sigma + k_3 S_m + k_4 S_\sigma \quad (1)$$

where L_m represents the mean average value of the support beam length, L_σ indicates the variance of the support beam length, S_m is the average value of the small area divided by the support beam, S_σ represents the variance of the small area divided by the support beam, and $k_1, k_2, k_3,$ and k_4 are weight coefficients. Minimization of the objective function is undertaken with the aim of minimizing the length of the support beams and ensure

small, uniform divided areas. When discretizing m points and designing n support lines, the computation is initially $O(nm^2)$, demanding significant computational resources. To address this, an accelerated algorithm is devised to streamline the calculation complexity to $O(nm)$. When $m = 20$, $n = 10$, employing the acceleration algorithm, the computation time is 240 s on a computer equipped with an i7-11700k CPU and 8 GB of RAM.

2.2. Deformation Compensation of Support Beam

In addressing the challenge of support beam deformation induced by gravity, this paper proposes a methodology by which to construct a deformation model for extruded wire under gravitational influence. Subsequently, the compensation track is computed based on the designed trajectory. Illustrated in Figure 4, the anticipated trajectory is denoted as S_0 ; however, due to the impact of gravity, the printed trajectory deviates to S_1 from the intended S_0 . To rectify this deformation, the compensation track S_2 is calculated, aiming to achieve a post-printing trajectory as closely aligned with S_0 as possible.

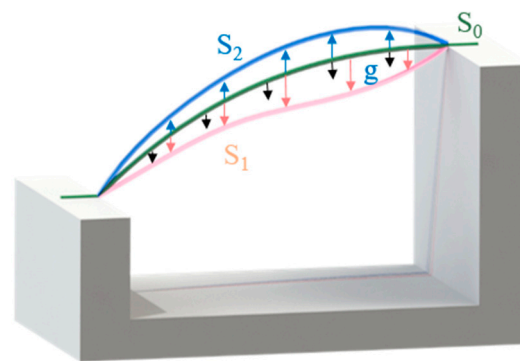


Figure 4. A schematic diagram illustrating the deformation of the printing wire.

The deformation process of a suspended extrusion wire is analyzed to establish a comprehensive deformation model. The deformation characteristics of the extruded wire are delineated as follows: upon initial extrusion, the wire exhibits the lowest degree of solidification, resulting in the maximum falling deformation. Subsequently, as the wire gradually solidifies, the deformation diminishes. Even fully cured wire is subject to the residual deformation of the freshly extruded wire from the print head, with the initial fixed end resisting deformation. In the paper, the impact of various printing materials, extrusion temperatures, and extrusion speeds on the printing process is abstracted into model coefficients. The modeling conditions for the deformation model assume constant printing materials, extrusion temperatures, and extrusion speeds. Different printing materials, extrusion temperatures, and extrusion speeds result in distinct coefficients within the deformation model; however, the deformation patterns of all cases can be described using the deformation model. In cases where the extrusion speed of the wire is lower than the scanning speed, the wire experiences viscoelastic forces, induced by the nozzle. Conversely, if the wire's extrusion speed exceeds the scanning speed, it accumulates at the nozzle's extrusion point. During printing, the wire's extrusion speed is adjusted to align with the scanning speed. Consequently, the modeling process neglects the wire deformation resulting from mismatches between the extrusion and scanning speeds. The mathematical representation of the wire deformation law is detailed as follows:

$$\vec{\Delta S} = \left(k \times \vec{g} \times e^{\left(\frac{-\|i-t\|^2}{\sigma_1}\right)} \right) \times \left(1 - e^{\left(\frac{-\|i-t\|^2}{\sigma_2}\right)} \right) \quad (2)$$

where, k represents the gravitational coefficient, \vec{g} denotes the gravitational vector, i signifies the discrete current point on the printing trajectory, t corresponds to the point on the printing trajectory associated with the discrete position of the nozzle, σ_1 represents the

influence coefficient of the freshly extruded material on the current point, and σ_2 denotes the influence coefficient of the fixed end on the current point.

In the above formula, the first bracket characterizes the impact of the freshly extruded wire on the current point, while the final bracket delineates the influence of the fixed end on the current point. As illustrated in Figure 5, all points ranging from point i to point t contribute to the downward deformation of point i . The fixed point serves to resist the deformation influence on point i . Proximity to point i amplifies the impact on the deformation, with the greatest effect occurring when i is close to t , due to the newly extruded wire. Conversely, when i is in proximity to the fixed point, the deformation approaches zero.

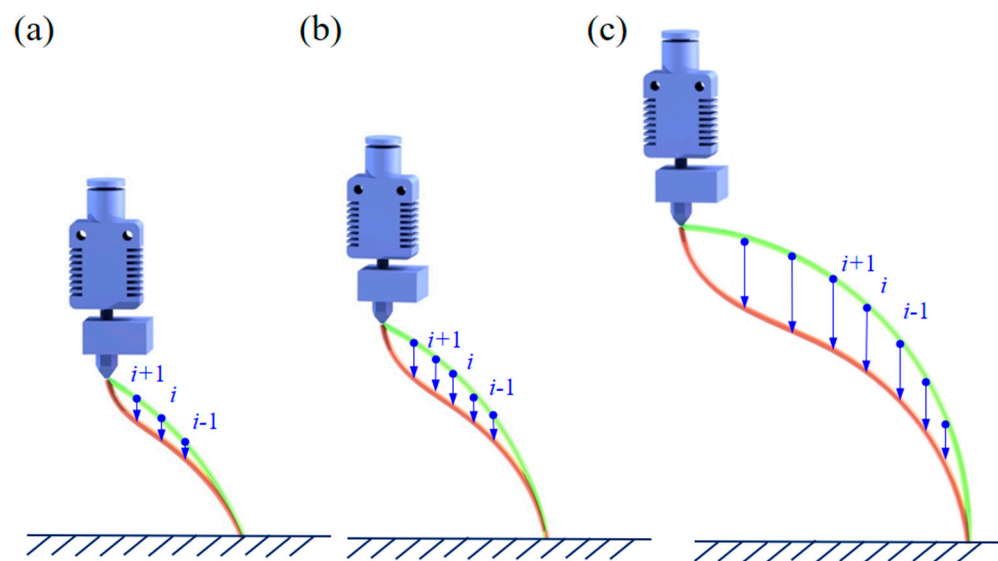


Figure 5. The deformation characteristics of printed wire. The wire experiences the greatest deformation immediately after extrusion from the nozzle, with the deformation decreasing as it approaches the fixed end. The process from (a–c) demonstrates the generation of deformation on printed lines.

The parameters to be derived in the formula include k , σ_1 , and σ_2 . These values are determined through the measurement of the actual deformation of the printed wire during experimentation. Once obtained, these parameters are input into the model, and the simulated print track should closely align with the experimental track. This constitutes the underlying principle behind the construction of the objective function in the parameter-solving process. It is important to emphasize that the deformation measured at point i during the experiment is denoted as ΔSR_i , the deformation in the model simulation is ΔS_i , and the deformation from point j to point i is ΔS_{ij} . Therefore:

$$S_i = \sum_i^t S_{ij} \quad (3)$$

The formulated objective function is presented as follows:

$$F(k, \sigma_1, \sigma_2) = \sum_1^n (\Delta S_i - \Delta SR_i)^2 \quad (4)$$

The motion accuracy of the printing device used in this study is approximately 0.5 mm. Given this, 0.5 mm is considered the acceptable error standard when the abovementioned objective function converges. Observing the aforementioned formula, it becomes evident that the objective function is highly intricate and exhibits robust nonlinearity. In this study, the differential evolution algorithm [25] is employed for the optimization of the objective function and resolution of the model parameters. The differential evolution algorithm is characterized by robust global convergence and stability.

(1) Population Initialization:

M individuals are randomly generated within the solution space, with each individual representing a potential solution to the problem. These individuals are recorded as:

$$X_i(0) = (x_{i,1}(0), x_{i,2}(0), x_{i,3}(0), \dots, x_{i,n}(0)) \quad (5)$$

$$i = 1, 2, 3, \dots, M$$

The j -dimensional value of the i -th individual is defined as follows:

$$X_{i,j}(0) = L_{j_min} + rand(0, 1)(L_{j_max} - L_{j_min}) \quad (6)$$

$$i = 1, 2, 3, \dots, M$$

$$j = 1, 2, 3, \dots, n$$

where L_{j_min} and L_{j_max} are the minimum and maximum values of the individual's j -dimensional value, respectively.

(2) Variation:

During the g -th iteration, three individuals were randomly chosen from the population, as follows:

$X_{p1}(g), X_{p2}(g), X_{p3}(g), p1 \neq p2 \neq p3 \neq i$. The generated variation vector is:

$$H_i(g) = X_{p1}(g) + f \cdot (X_{p2}(g) - X_{p3}(g)) \quad (7)$$

where f is the scaling factor.

(3) Cross:

$$v_{i,j} = \begin{cases} h_{i,j}(g), & rand(0, 1) \leq cr \\ x_{i,j}(g), & else \end{cases} \quad (8)$$

where $cr \in [0, 1]$ is the crossover probability.

(4) Selection:

$$X_i(g+1) = \begin{cases} V_i(g), & f(V_i(g)) < f(X_i(g)) \\ X_i(g), & else \end{cases} \quad (9)$$

For each individual, $X_i(g+1)$ is either better or equal to $X_i(g)$, and all optima are realized through mutation, crossover, and selection. In the context of the problem addressed in this paper, each individual in the population is represented as (k, σ_1, σ_2) . Figure 6 depicts the convergence process involved in solving model parameters using the differential evolution algorithm, with a population size of 50. After 460 generations of solutions, the model parameters essentially converge.

With the established deformation model and the anticipated trajectory, the deformation at each point along the wire can be computed. Compensation is then applied to each point to align the compensated trajectory as closely as possible with the anticipated trajectory. As illustrated in Figure 7, to ensure synchronization between the extrusion speed of the print compensation track and the scanning speed, the angle formed every two points after trajectory discretization with the x -axis selected as the compensation parameter. Initially, the model calculates the angle change of the wire after printing based on the uncompensated track. Subsequently, this angle change is multiplied by a scaling factor to derive the compensation, denoted as $\Delta\theta$. Finally, the optimal scaling factor is determined through a dichotomy process.

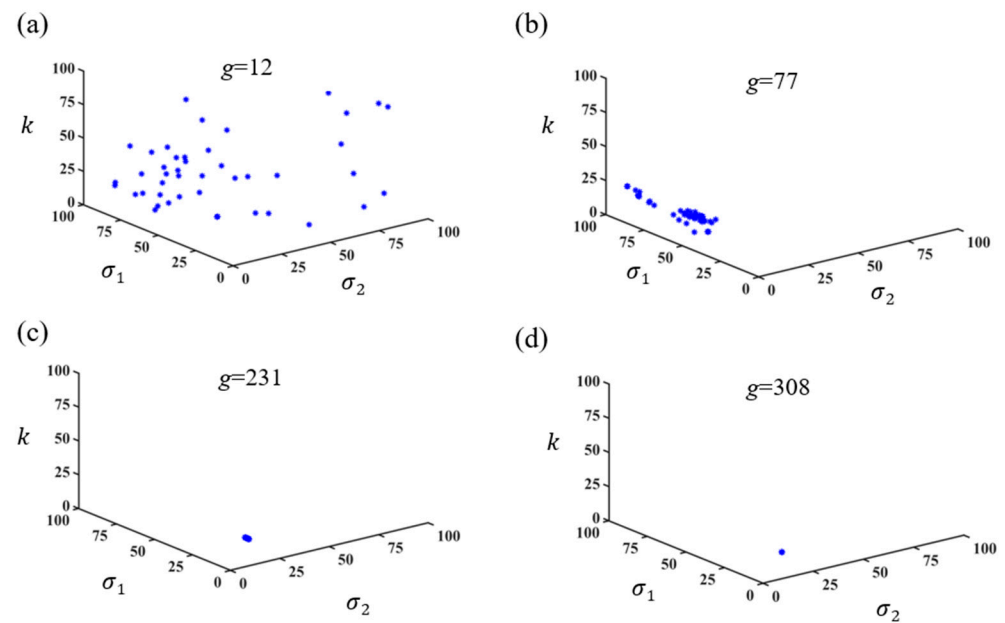


Figure 6. The convergence process for resolving model coefficients using the differential evolution algorithm. The convergence of the model coefficients using the difference algorithm is shown from (a–d), with 12 iterations, 77 iterations, 231 iterations, and 308 iterations, respectively.

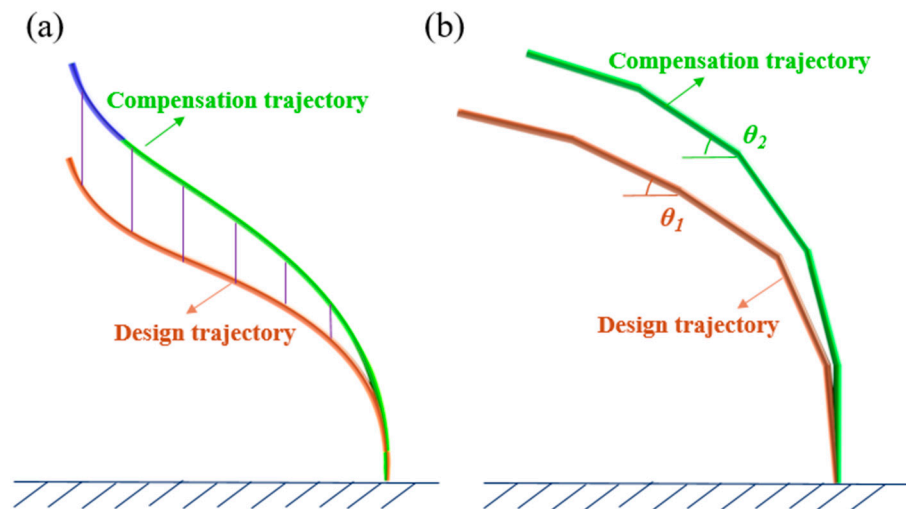


Figure 7. Different compensation strategies result in varying lengths of the print tracks. (a) Vertical compensation, where the blue track indicates a compensation track longer than the original track. (b) Angle-based compensation, with the length of the compensation track equal to that of the original track.

2.3. Experimental Equipment

Most repaired objects involve spatial surfaces, and conventional commercial printers often fail to meet the printing demands associated with spatial trajectory and nozzle rotation attitude. In this study, a developed 6-axis parallel printer [26], depicted in Figure 8, offers the flexibility to adjust the spatial pose of the nozzle, enabling effective surface repair.

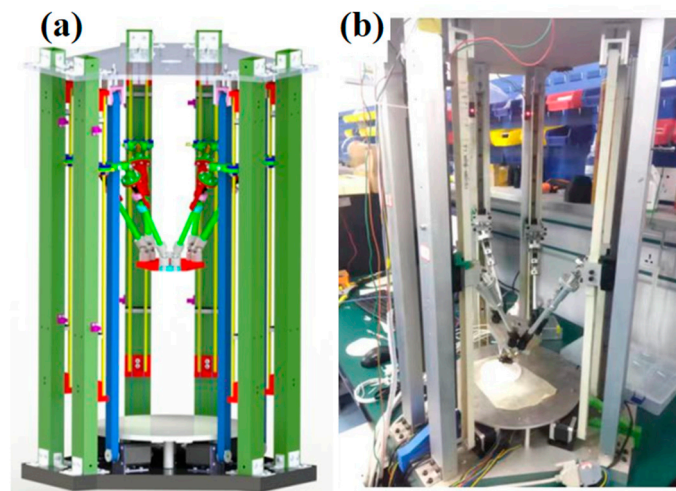


Figure 8. A six-axis printing device utilized for the repair study in the paper. (a) Three-dimensional model of the device. (b) Physical representation of the device.

3. Results and Discussion

The distribution of support beams is determined by an objective function that comprehensively considers the mean and variance of support beam length, as well as the mean and variance of the areas divided by the support beams. The various coefficients in the objective function correspond to different distributions of the support beams. Figure 9a illustrates the distribution of support beams obtained by solely considering the mean and variance of support beam length in the objective function. In this scenario, the support beams are arranged in proximity to the projected contour. Figure 9b displays the results aimed at achieving the smallest average area and the shortest average length of segmentation lines. This results in the program favoring the use of intersecting lines to segment the area as much as possible, disregarding the uniformity of the segmented area. Figure 9c illustrates the outcomes achieved by comprehensively considering the minimization of both the average area and variance of segmentation, as well as the minimization of the average length of segmentation lines. This approach successfully achieves our goal of evenly segmenting the given area as much as possible. For different contours in practical repair scenarios, the objective function coefficients can be adjusted accordingly to achieve the desired distribution of support beams. In Figure 9, segmentation lines are mapped from the plane to the curved surface, segmenting the curved surface. The uniformity of segmented areas on the curved surface may potentially decrease. However, in practice, this phenomenon can be mitigated by adjusting the relative positions of the plane and the curved surface as much as possible.

The experimental printing material utilized in this study is PLA, with an extrusion temperature set at 210 °C. The filamentous material exhibits a diameter of 1.75 mm, while the printing nozzle diameter is 0.8 mm. The extruder operates at a speed of 2 rad/s, while the nozzle movement speed is maintained at 3 mm/s. Notably, due to a marginally higher material intake rate into the nozzle per unit time compared with the extrusion speed, the resultant actual extrusion line width average diameter surpasses that of the nozzle diameter.

The printing experiment aimed at investigating the deformation model of the supporting beam was conducted as follows: initially, a 10 mm straight line was printed on the printer base plate to serve as the fixed end for subsequent suspended printing. Subsequently, printing proceeded according to the suspended trajectory. Upon completion of printing, the nozzle remained stationary for a 10 s interval to facilitate cooling and shaping of the printed wire. To ensure data reliability and experiment repeatability, 30 sets of samples were printed following a 1/4 arc trajectory with a radius of 30 mm. The deformation of each set of samples relative ideal trajectory was measured using a parallel light monocular camera. From these, 24 sets of sample deformation values were randomly selected as

calculation data for the deformation model coefficients discussed in the article, while the remaining 6 sets were designated as test data.

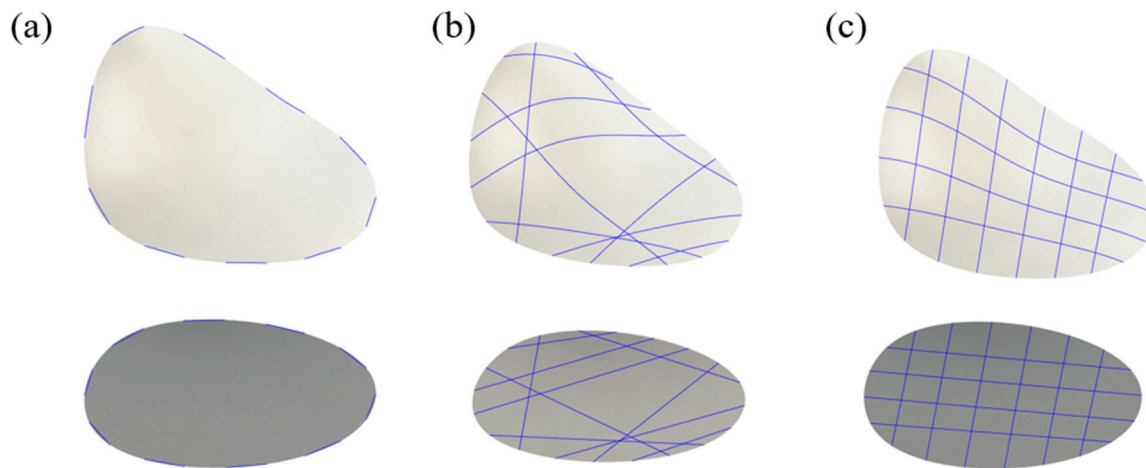


Figure 9. Distinct coefficients in the objective function yield varying distributions of support beams. (a) Outcomes when solely considering the average length of the dividing line. (b) Results incorporating both the average length of the dividing line and the mean dividing area. (c) Comprehensive consideration of the average length of the dividing line, the mean, and the variance of the dividing area.

Figure 10 presents the outcomes when resolving the deformation model coefficients using experimental data and the differential evolution algorithm. In the paper, printing was conducted following a designed quarter-circle trajectory with a radius of 30 mm. A parallel light camera was employed to measure the actual deformation of the printed filament, obtaining discrete coordinate values as fitting data for the coefficients of the deformation model and serving as test data. The figure illustrates the average and standard deviation of both the training and testing data. Inspection of the graph reveals a close alignment between the trajectory derived from the deformation model and the distribution of data employed when solving the model coefficients. This alignment indicates the convergence of the solution results for the model coefficients. Furthermore, the trajectory derived from the deformation model demonstrates a strong concordance with the testing data, thereby providing additional validation of the model's generalization capacity. The simulation trajectory exhibits notable agreement with the experimental data, with a calculated average error of less than 0.3 mm, indicating that the deformation model can accurately describe the deformation process.

The process of formulating a deformation model suggests that its applicability is not contingent upon the specific shape of the trajectory. With varying ideal trajectories, these deformation models possess the capability to prognosticate the corresponding deformation magnitudes. To ascertain the generalization prowess of the trajectory-independent deformation model, printing experiments were conducted employing diverse trajectories. Subsequently, the deformation amounts of the samples were compared with those calculated by the model. To uphold data reliability and experiment reproducibility, 10 samples were iteratively printed for each trajectory, and the resultant average value was adopted as the experimental data. Figure 11 illustrates the simulation and compensation outcomes for arcs, straight lines, and splines with varying diameters using the deformation model. The deformation model coefficients are derived from the experimental data of straight-line printing for an R30 arc but are applied to other printing trajectories. As depicted in the figure, the simulation track remains in good agreement with the experimental data. Utilizing the aforementioned compensation method, the wire printed according to the compensation track closely aligns with the expected trajectory.

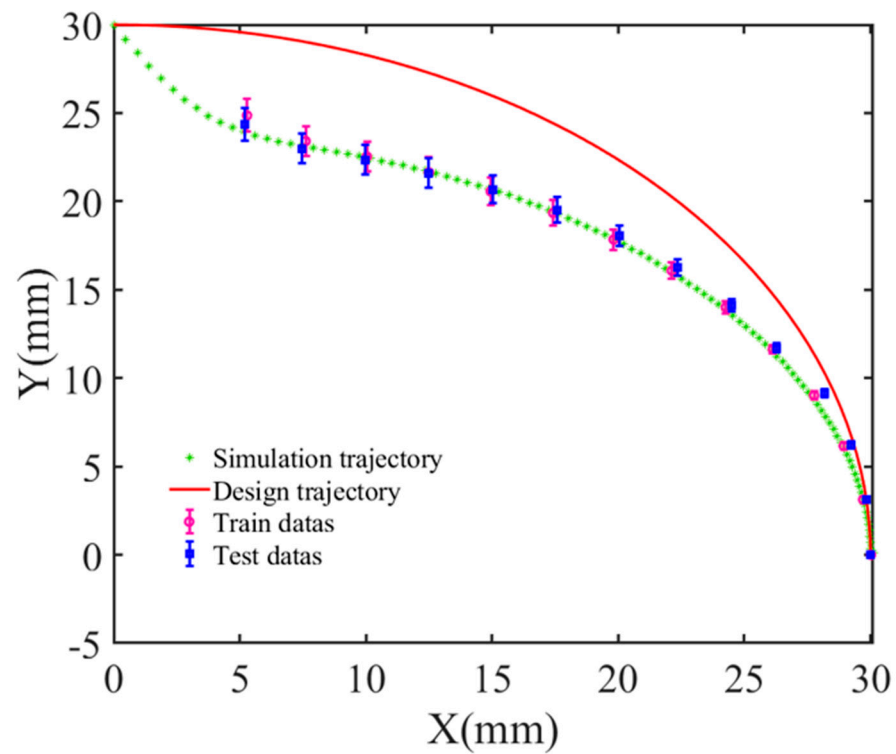


Figure 10. The print trajectory's deformation is simulated using the resolved model and subsequently compared with the experimental data.

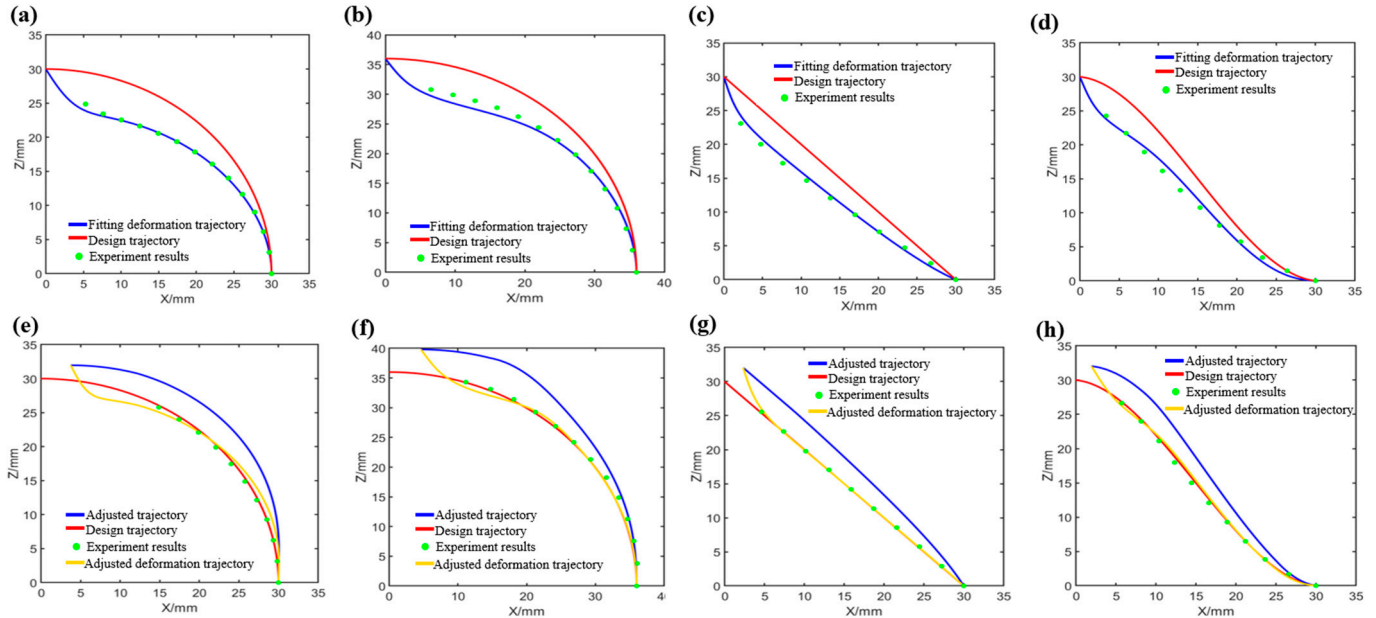


Figure 11. The simulation and compensation of deformation for circular arcs, straight lines, and spline curves are conducted and subsequently compared with experimental data. Respectively, (a–d) present the fitting results of the calculated model for trajectories with a radius of 30 mm arc, a radius of 35 mm arc, a straight line, and a spline curve. Respectively, (e–h) illustrate the deformation of sampling points for trajectories with a radius of 30 mm arc, a radius of 35 mm arc, a straight line, and a spline curve after employing the compensation strategy.

Utilizing deformation models and compensation strategies, the printing trajectory is systematically adjusted to mitigate the deformation of printed lines. The study conducts

compensation experiments on a 1/4 arc trajectory with a radius of 30 mm. To uphold data reliability and experimental reproducibility, three compensation experiments were executed. Subsequently, the deformation of the compensated printed samples was measured, and their average and standard deviation were calculated. These statistical outcomes were then juxtaposed with the uncompensated experimental data comprising 30 sets for comparative analysis. Figure 12 presents the statistical outcomes depicting the deviation between the support beam and the ideal track after printing, according to the compensated track and the uncompensated track. From the depicted graph, it becomes evident that the deformation of the printing area in the uncompensated sample amplifies with its progression towards the rear. This phenomenon arises because the printing area, situated farther away from the fixed end, experiences diminished resistance to deformation from the fixed end and becomes increasingly susceptible to gravitational forces. Statistical analysis revealed that the maximum average deformation of the uncompensated sample approximates 5.20 mm. This degree of deformation exceeds the width of the printed lines significantly, potentially resulting in inadequate bonding between adjacent printed materials. Following compensation, the deformation across the entire trajectory of the printed sample notably diminishes. According to statistical findings, the maximum deformation of the sampled points post-compensation measures approximately 0.15 mm. Consequently, the maximum deformation of the printed sample post-compensation is reduced to about 3% of its pre-compensation magnitude. The results indicate that the deformation model and compensation method proposed in this article effectively mitigate the impact of gravity-induced deformation on the printing lines. Simulation and experimental results collectively affirm the efficacy of the deformation model and the support beam compensation method.

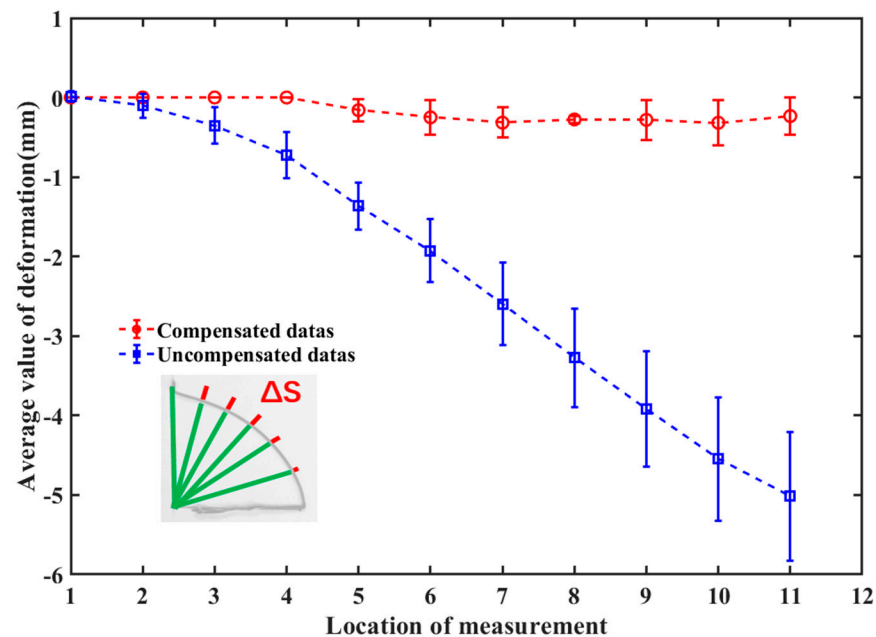


Figure 12. Comparison of deformation between compensated print and uncompensated print tracks.

Printing on a support beam that compensates for deformation can effectively mitigate the deformation of the repaired part, thereby ensuring the structural integrity of the component. To this end, repair experiments were conducted on damaged components following the process outlined in Figure 2. This process involves initially performing a 3D scan of the damaged parts and subsequently isolating the damaged area. Next, the trajectory of the support beam and the repair trajectory within the damaged area are planned. In order to quantitatively evaluate the repair outcomes, the study designed a hat-shaped component, specifying the shape of the damage. The three-dimensional shapes of both the damaged model and the ideal model are well-defined, serving as reference

data for the repair process and subsequent assessment of repair results. Figure 13a,b display the printed results of the support beam and the covering layer on the support beam, respectively. The printing results reveal variations in the thickness of certain beams due to material heterogeneity. However, this does not compromise the effectiveness of compensatory beams in reducing layer deformation. Another observed phenomenon based on the printing results is that there is some interaction between the beams. Specifically, the upper layer support beams exhibit less deformation than the lower layer, implying that subsequently printed support beams have smaller deformations than those printed earlier. This insight provides inspiration for support beam distribution and printing sequences. Overall, the role of support beams significantly reduces the difficulty of repairs, verifying the feasibility of the FDM repair strategy.

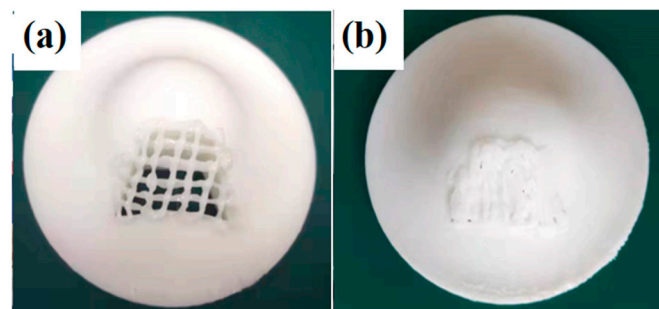


Figure 13. (a) The printed results of the support beams. (b) The printed results of the overlay.

During the experiment, a structured light scanner was employed to capture the point cloud of the repaired parts. Figure 14 compares the repair outcomes of damaged samples using the strategy proposed in this paper against direct repair. Point clouds of the repaired parts were obtained, and the distance between these point clouds and the surface of the undamaged part model was calculated. As illustrated in Figure 14c,d, the mean distance between the point clouds of the repaired parts using the proposed repair strategy is 0.197 mm and the intact model surface is noticeably less than the mean distance corresponding to direct repair, at 0.830 mm. The repair error with compensatory support beams was found to be 76% lower than that without compensatory support beams. In essence, the deformation of the parts repaired by the proposed strategy is significantly smaller than that of the original model. Moreover, the comparison results indicate that the printed lines in direct repair, prone to deformation, struggle to adhere tightly, resulting in numerous holes in the repair area and ultimately leading to repair failure. One point to note is that the repair layer covers the damaged area, leading to noticeable repair traces. This can be mitigated by grinding the area around the damaged contours of the part before the repair.

The experimental results indicate that the proposed repair method using compensatory beams provides an effective approach for the restoration of extensively damaged curved surface components. This differs from previous additive repair studies primarily in two aspects. Firstly, conventional studies often focus on repairing components with small-scale damage features such as pits and cracks, which can be directly addressed by adding material to the damaged part. However, the studied damage features in this paper involve large-scale perforations in curved surface shells, making it impractical to repair by simply adding material to the damaged area. Secondly, the paper presents, for the first time, a precise modeling of the deformation patterns of unsupported beams, significantly enhancing accuracy when repairing part dimensions. Previous research has primarily emphasized repair strength, often resorting to subtractive processing for dimension adjustment after repair. The compensatory repair method proposed in this paper demonstrates the potential for one-time, precision repair of damaged parts without the need for subsequent processing.

Through experiments and simulations, it has been confirmed that the FDM repair strategy for damaged surfaces can effectively restore the surface with minimal deformation. However, it is important to note that the exploration of bonding strength between the

repaired area and the damaged part is not the primary focus of this article. This intriguing topic will be the subject of our next comprehensive investigation.

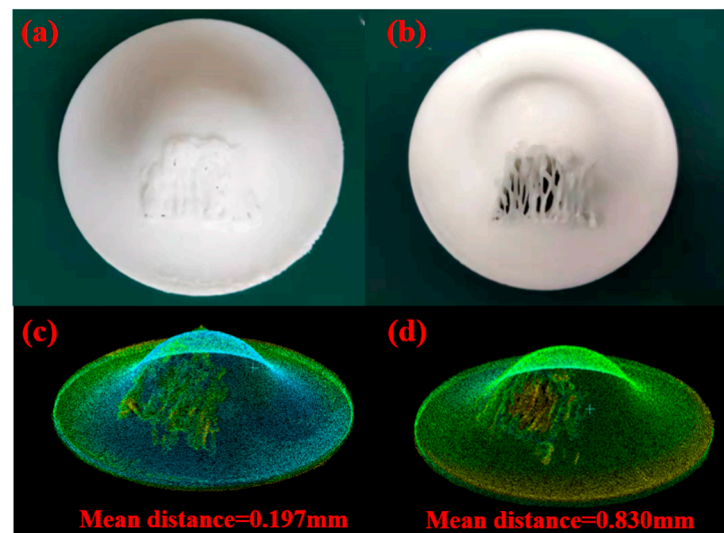


Figure 14. Comparison between the results printed using the support beam repair strategy and direct repair. (a) The result achieved through the utilization of support beams in the repair process. (b) The outcome of direct repair without the incorporation of support beams. (c) The 3D point cloud representation illustrating the results of repair with the implementation of support beams. (d) The point cloud visualizations depicting the results of repair without the utilization of support beams.

4. Conclusions

Focusing on damaged polymer parts, this study introduces a novel FDM repair method involving the sequential printing of support beams followed by the cover layer. In the paper, deformation trajectories were modeled, and methods for calculating the distribution of supporting beams were introduced. The proposed method in the paper addresses the challenging issue of additive repair for large-area damaged curved surfaces, offering new possibilities for in-situ repairs in scenarios where adding support is not feasible, such as in the additive repair of human skull bones. Moreover, the proposed process endeavors to achieve more precise repair outcomes for the morphology in a single step, thereby streamlining the conventional repair approach that involves the sequential addition and reduction of materials. Experimental findings indicate that the maximum average deformation of the uncompensated line measures approximately 5.20 mm, while the maximum deformation of the compensated line sampling points is approximately 0.15 mm. Following compensation, the maximum deformation of the suspended printed line diminishes to approximately 3% of its pre-compensation magnitude. The mean distance between the point clouds of the repaired parts using the proposed repair strategy is 0.197 mm and the intact model surface is noticeably less than the mean distance corresponding to direct repair, at 0.830 mm. The repair error with compensatory support beams was found to be 76% lower than that without compensatory support beams. The proposed repair strategy significantly outperforms direct repair in terms of repair integrity and deformation. To fully exploit the potential of the proposed method, research on online detection, real-time trajectory generation methods, and in-situ printing processes for additive repair will be the focal point of our subsequent research efforts.

Author Contributions: Conceptualization, D.Z. and B.G.; Methodology, D.Z.; Validation, D.Z.; Data curation, D.Z.; Writing – original draft, D.Z.; Writing – review & editing, B.G.. All authors have read and agreed to the published version of the manuscript.

Funding: This research is supported by the National Natural Science Funds of China No. 51975142.

Data Availability Statement: No new data were created or analyzed in this study. Data sharing is not applicable to this article.

Acknowledgments: I extend my gratitude to Teacher Guo Bin for his invaluable guidance in problem exploration and experimental implementation.

Conflicts of Interest: The authors declare that they have no known competing financial interests or personal relationships that could have appeared to influence the work reported in this paper.

References

1. Fidan, I.; Huseynov, O.; Ali, M.A.; Alkunte, S.; Rajeshirke, M.; Gupta, A.; Sharma, A. Recent inventions in additive manufacturing: Holistic review. *Inventions* **2023**, *8*, 103. [[CrossRef](#)]
2. Chadha, U.; Abrol, A.; Vora, N.P.; Tiwari, A.; Shanker, S.K.; Selvaraj, S.K. Performance evaluation of 3D printing technologies: A review, recent advances, current challenges, and future directions. *Prog. Addit. Manuf.* **2022**, *7*, 853–886. [[CrossRef](#)]
3. Kanishka, K.; Acherjee, B. A systematic review of additive manufacturing-based remanufacturing techniques for component repair and restoration. *J. Manuf. Process.* **2023**, *89*, 220–283. [[CrossRef](#)]
4. Zhao, Y.; Lian, Y.; Li, L.; Gong, X.; Chai, X.; Liu, W. Vibration test method of aero-engine 3D printing pre-swirl nozzle based on equivalent installation stiffness. *J. Mech. Sci. Technol.* **2023**, *37*, 617–630. [[CrossRef](#)]
5. Ziólkowski, M.; Dyl, T. Possible applications of additive manufacturing technologies in shipbuilding: A review. *Machines* **2020**, *8*, 84. [[CrossRef](#)]
6. Slavin, B.V.; Ehlen, Q.T.; Costello, J.P.; Nayak, V.V.; Bonfante, E.A.; Benalcázar Jalkh, E.B.; Coelho, P.G. 3D Printing Applications for Craniomaxillofacial Reconstruction: A Sweeping Review. *ACS Biomater. Sci. Eng.* **2023**, *9*, 6586–6609. [[CrossRef](#)] [[PubMed](#)]
7. Liu, S.; Li, Y.; Li, N. A novel free-hanging 3D printing method for continuous carbon fiber reinforced thermoplastic lattice truss core structures. *Mater. Des.* **2018**, *137*, 235–244. [[CrossRef](#)]
8. Dong, K.; Liu, L.; Huang, X.; Xiao, X. 3D printing of continuous fiber reinforced diamond cellular structural composites and tensile properties. *Compos. Struct.* **2020**, *250*, 112610. [[CrossRef](#)]
9. Li, N.; Link, G.; Wang, T.; Ramopoulos, V.; Neumaier, D.; Hofele, J.; Walter, M.; Jelonnek, J. Path-designed 3D printing for topological optimized continuous carbon fibre reinforced composite structures. *Compos. Part B Eng.* **2020**, *182*, 107612. [[CrossRef](#)]
10. De Marzi, A.; Vibrante, M.; Bottin, M.; Franchin, G. Development of robot assisted hybrid additive manufacturing technology for the freeform fabrication of lattice structures. *Addit. Manuf.* **2023**, *66*, 103456. [[CrossRef](#)]
11. Ouyang, Z.; Yang, L.; Pi, Z.; Wang, Z.; Yan, C.; Shi, Y. Robot-assisted laser additive manufacturing for high-strength/low-porosity continuous fiber-reinforced thermoplastic composites. *Compos. Sci. Technol.* **2024**, *247*, 110397. [[CrossRef](#)]
12. Bhatt, P.M.; Malhan, R.K.; Shembekar, A.V.; Yoon, Y.J.; Gupta, S.K. Expanding capabilities of additive manufacturing through use of robotics technologies: A survey. *Addit. Manuf.* **2020**, *31*, 100933. [[CrossRef](#)]
13. Merz, B.; Poka, K.; Nilsson, R.; Mohr, G. Hilgenberg, On the challenges of hybrid repair of gas turbine blades using laser powder bed fusion. *Lasers Manuf. (LiM)* **2023**, *2023*, 1–9.
14. Hamilton, J.D.; Sorondo, S.; Li, B.; Qin, H.; Rivero, I.V. Mechanical behavior of bimetallic stainless steel and gray cast iron repairs via directed energy deposition additive manufacturing. *J. Manuf. Process.* **2023**, *85*, 1197–1207. [[CrossRef](#)]
15. Saboori, A.; Aversa, A.; Marchese, G.; Biamino, S.; Lombardi, M.; Fino, P. Application of directed energy deposition-based additive manufacturing in repair. *Appl. Sci.* **2019**, *9*, 3316. [[CrossRef](#)]
16. Lang, F.; Schmitt, J.C.; Cabeza, S.; Pirling, T.; Fiebig, J.; Vassen, R.; Gibmeier, J. IN718 Cold Gas Repair Spray of Large Cavities—Microstructure and Residual Stresses. In *TMS Annual Meeting & Exhibition*; Springer Nature: Cham, Switzerland, 2023; pp. 739–753.
17. Martin, L.P.; Luccitti, A.; Walluk, M. Repair of aluminum 6061 plate by additive friction stir deposition. *Int. J. Adv. Manuf. Technol.* **2021**, *118*, 759–773. [[CrossRef](#)]
18. Rahmatabadi, D.; Ghasemi, I.; Baniassadi, M.; Abrinia, K.; Baghani, M. 4D printing of PLA-TPU blends: Effect of PLA concentration, loading mode, and programming temperature on the shape memory effect. *J. Mater. Sci.* **2023**, *58*, 7227–7243. [[CrossRef](#)]
19. Rahmatabadi, D.; Ghasemi, I.; Baniassadi, M.; Abrinia, K.; Baghani, M. 3D printing of PLA-TPU with different component ratios: Fracture toughness, mechanical properties, and morphology. *J. Mater. Res. Technol.* **2022**, *21*, 3970–3981. [[CrossRef](#)]
20. Rahmatabadi, D.; Ghasemi, I.; Baniassadi, M.; Abrinia, K.; Baghani, M. Development of Pure Poly Vinyl Chloride (PVC) with Excellent 3D Printability and Macro-and Micro-Structural Properties. *Macromol. Mater. Eng.* **2023**, *308*, 2200568. [[CrossRef](#)]
21. Chennakesava, P.; Narayan, Y.S. Fused deposition modeling-insights. In *Proceedings of the International Conference on Advances in Design and Manufacturing ICAD&M*, Tamil Nadu, India, 5–7 December 2014; p. 1345.
22. Borsuk, K. *Foundations of Geometry*; Courier Dover Publications: New York, NY, USA, 2018.
23. Strikwerda, J.C. *Finite Difference Schemes and Partial Differential Equations*; Society for Industrial and Applied Mathematics: Philadelphia, PA, USA, 2004.
24. Lydia, A.; Francis, S. Adagrad—An optimizer for stochastic gradient descent. *Int. J. Inf. Comput. Sci.* **2019**, *6*, 566–568.

-
25. Price, K.V. Differential evolution. In *Handbook of Optimization: From Classical to Modern Approach*; Springer: Berlin/Heidelberg, Germany, 2013; pp. 187–214.
 26. Zhang, D.; Zhang, G.; Li, L. Calibration of a six-axis parallel manipulator based on BP neural network, *Industrial Robot. Int. J. Robot. Res. Appl.* **2019**, *46*, 692–698. [[CrossRef](#)]

Disclaimer/Publisher’s Note: The statements, opinions and data contained in all publications are solely those of the individual author(s) and contributor(s) and not of MDPI and/or the editor(s). MDPI and/or the editor(s) disclaim responsibility for any injury to people or property resulting from any ideas, methods, instructions or products referred to in the content.